Journal of Biomedical Optics

SPIEDigitalLibrary.org/jbo

In vivo full-field *en face* correlation mapping optical coherence tomography

Paul M. McNamara
Hrebesh M. Subhash
Martin J. Leahy

SPIE

In vivo full-field *en face* correlation mapping optical coherence tomography

Paul M. McNamara,[a] Hrebesh M. Subhash,[a] and Martin J. Leahy[a,b]
[a]National University of Ireland, Tissue Optics and Microcirculation Imaging Facility, National Biophotonics and Imaging Platform, Galway, Ireland
[b]RCSI Royal College of Surgeons, 123 St. Stephens Green, Dublin 2, Ireland

Abstract. A full-field optical coherence tomography (OCT) system has been developed for the purpose of performing nonscanning *en face* flow imaging. The light source is centered at 840 nm with a bandwidth of 50 nm resulting in an axial resolution of 8 μm in air. Microscope objectives with a numerical aperture of 0.1 were incorporated giving a transverse resolution of 5 μm. A magnification of 5.65 was measured, resulting in a field of view of 1260×945 μm. Pairs of interference fringe images are captured with opposing phase and a two-step phase image reconstruction method is applied to reconstruct each *en face* image. The OCT frame rate is 10 Hz. A two-dimensional cross-correlation technique is applied to pairs of consecutive *en face* images in order to distinguish dynamic from static light-scatterers. The feasibility of the method was examined by simulating blood flow by creating a phantom with 5% intralipid solution. *In vivo* imaging of a *Xenopus laevis* tadpole was also performed in order to investigate the feasibility of imaging the vascular system. We present for what we believe to be the first time, the application of correlation mapping optical coherence tomography to full-field OCT to provide *in vivo* functional imaging of blood vessels. [DOI: 10.1117/1.JBO.18.12.126008]

Keywords: optical coherence tomography; full-field; *en face*; video rate; blood flow; imaging; correlation mapping.

Paper 130622LR received Aug. 26, 2013; revised manuscript received Nov. 11, 2013; accepted for publication Nov. 15, 2013; published online Dec. 16, 2013.

1 Introduction

Optical coherence tomography (OCT) is a recently developed optical technique which has the ability to noninvasively visualize three-dimensional (3-D) structural information of a biological sample on the micron scale.[1] Generally, the method is based on a Michelson-type interferometric set-up which utilizes a broadband light source to coherence-gate the light returning from a sample and hence provide high axial resolution. OCT has been utilized in many biological applications including ophthalmology, cardiology, oncology, neurology, dermatology, etc. Full-field OCT is an alternative coherence domain imaging modality which, unlike conventional OCT, produces tomographic images in the *en face* orientation (i.e., orthogonal to the optical axis).[2] This modality utilizes a charge-coupled device (CCD) or complementary metal-oxide-semiconductor (CMOS) camera to capture the full-field at a particular depth, negating the necessity for lateral scanning.[3] The axial resolution is set by the bandwidth of the light source used (as is the case with all modalities of OCT), and the transverse resolution is set by the choice of optical components on the reference and sample arms. This means that transverse resolutions similar to that of conventional microscopy ($\sim$1 μm) are easily achievable, which has led to numerous studies on cellular-level tomographical imaging in both *ex vivo*[4,5] and *in vivo*[6,7] imaging applications.

Various methods of image reconstruction have been reported with, generally, a trade-off of speed of image acquisition and system sensitivity.[8] In this work, the aim is to utilize spatial and temporal correlations in successive frames in order to extract flow information. For this reason, speed of acquisition is a priority and hence a two-step method is employed in conjunction with the mathematical Hilbert transform to reconstruct each *en face* image.[9]

The correlation mapping optical coherence tomography (cmOCT) processing algorithm was developed by our group[10,11] and utilizes the time-varying speckle effect produced from moving scatterers to provide contrast against static tissue. The technique has previously been applied to images acquired with frequency-domain OCT systems and hence in a cross-sectional geometry.[10–12] To our knowledge, this is the first instance of the application of cmOCT to the full-field modality of OCT. In the present study, full-field cmOCT is utilized to image a phantom in order to illustrate its ability to separate static structures from dynamic structures moving under Brownian motion. In addition, *in vivo* blood flow imaging of a *Xenopus laevis* tadpole is demonstrated.

2 Experimental Configuration and System Performance

A diagram of the experimental set-up is shown in Fig. 1(a). The light source for the set-up consists of a near-infrared super luminescent diode centered at 840 nm with a bandwidth of 50 nm (Superlum S-840B-I-20, Carrigtwohill, Co. Cork, Ireland). This light source has an output power of 15 mW with a double-Gaussian spectral profile. The incident light is input into the interferometer via a single mode optical fibre and is collimated into a beam with diameter of $\sim$10 mm using a doublet of focal length 50 mm. The purpose of collimation was to ensure uniform illumination of the sample. The beam splitter has a splitting ratio of 50 : 50 which splits the amplitude into the reference and sample

Address all correspondence to: Paul M. McNamara, National University of Ireland, Tissue Optics and Microcirculation Imaging Facility, National Biophotonics and Imaging Platform, Galway, Ireland. Tel: +353-91-492824; E-mail: paul.m.mcnamara@ul.ie

0091-3286/2013/$25.00

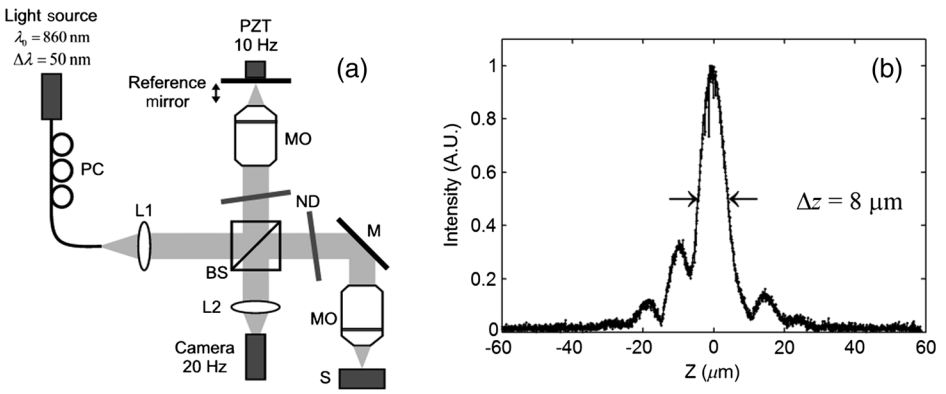

Fig. 1 (a) Schematic representation of the experimental set up. The light source is a super-luminescent diode. PC, polarization control; BS, beam splitter (50:50); MO, microscope objective (4 × NA = 0.1); L1 and L2, achromatic doublets (50 and 200 mm focal length, respectively); M, mirror for upright sample arm; ND, variable neutral density filters (optical density 0 to 2); S, sample and stage; PZT, piezoelectric actuator (oscillation of 10 Hz, peak-to-peak amplitude = $\lambda_0/4 = 0.21$ μm). (b) The axial response of a single pixel of each *en face* image measured by scanning a mirror in the axial direction. The axial resolution of the system = 8 μm.

signals. Two identical variable neutral density filters are placed in the paths of each of the beams in order to provide dispersion compensation and control the visibility of the interference pattern. Two identical microscope objectives [4× numerical aperture (NA) = 0.1 Olympus, UK, working distance = 18.5 mm] are placed on each arm to focus the beam onto the reference mirror and sample. All components are coated with the appropriate anti-reflection coating in order to reduce reflections coming from within the system.

The process of reconstructing the interferogram images involves use of the mathematical Hilbert transform, details of which can be found in Na et al.[9] A phase shift of π was provided by a piezoelectric transducer (PZT) which oscillates the reference mirror. The PZT system employed is a closed-loop system using a Physik Instrumente, Karlsruhe, Germany, piezo actuator (P-841.1) and amplifier (E-665). The camera model used is a Hamamatsu, Hertfordshire, UK, Orca Flash 2.8 (C11440), which incorporates a CMOS sensor consisting of 1920 × 1440 square pixels of size 3.63 μm and a 12-bit analogue-to-digital converter. The camera is triggered externally with a maximum frame-rate of 20 Hz. (Higher frame rates are possible at the expense of the amount of pixels utilized). Since a two-step image reconstruction algorithm is utilized, the PZT must operate at half the frequency of the camera meaning a maximum OCT frame-rate of 10 Hz. The signals to drive the PZT and the camera are provided by a National Instruments, Berkshire, UK, data acquisition system, which is controlled by LabVIEW allowing accurate synchronization.

The detection sensitivity and dynamic range of the system was measured experimentally by scanning a mirror through the focal plane of the sample microscope objective. A neutral density filter of optical density, $D = 1.1$, was placed in the path of the sample beam. The measured fringe intensity of a single pixel was plotted as a function of position and the dynamic range and sensitivity were measured from this graph. The detection sensitivity represents the noise floor of the system and was measured as the intensity of a single pixel, averaged over 100 points, at a position far from the zero-position and was found to be 61 dB. It is important to note that this test was done without averaging multiple frames at each position. The dynamic range was measured as the ratio between the highest and lowest signals measureable by the camera and was found to be 39 dB.

The axial resolution of the system, Δz, is equal to the "round-trip" coherence length of the light source. This was measured experimentally by using a mirror as the sample and scanning in the axial direction using a step-size of 0.1 μm. The signal from a single pixel of each *en face* (demodulated) image was plotted as a function of position and the full-width at half maximum was measured to be 8 μm [Fig. 1(b)]. The transverse resolution is determined by the NA of the microscope objectives and was measured experimentally by imaging a standard target (1951 U.S. Air Force). The smallest resolvable feature at this magnification was found to be Group 6, Element 6 (i.e., 4.39 μm). The overall magnification of the system was measured to be 5.65 resulting in a field of view of 1260 × 945 μm covered by the 1920 × 1440 pixels of the camera.

2.1 *Correlation Mapping*

The correlation mapping algorithm is applied to pairs of consecutive *en face* images. In order to suppress the decorrelation of noisy background pixels between consecutive frames, each image is first subject to a threshold algorithm which equates any pixel below the threshold value to zero. Finding the correlation map between frame A and frame B involves calculation of the two-dimensional (2-D) cross-correlation of a grid of size $M \times N$ from frame A with the corresponding grid in frame B using the equation:

$$\mathrm{cmOCT}(x,y) = \sum_{p=0}^{M-1}\sum_{q=0}^{N-1} \frac{\left[I_A(x+p,y+q) - \bar{I}_A(x,y)\right]\left[I_B(x+p,y+q) - \bar{I}_B(x,y)\right]}{\sqrt{[I_A(x+p,y+q) - \bar{I}_A(x,y)]^2[I_B(x+p,y+q) - \bar{I}_B(x,y)]^2}}, \quad (1)$$

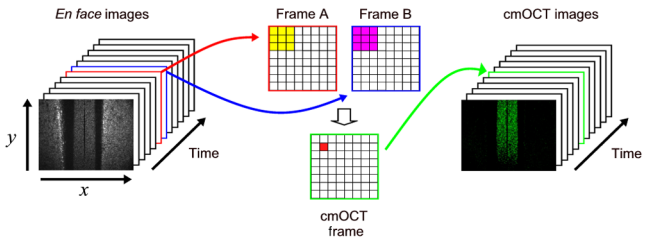

Fig. 2 Flow chart of the procedure of applying the correlation mapping algorithm to pairs of consecutive *en face* images. The two-dimensional cross-correlation is found between a grid (illustrated as 3×3) in frame A and frame B and repeated by stepping the grid across the whole range of the image. The process is repeated for all consecutive pairs of *en face* images.

where $\bar{I}$ is the grid's mean value. The grid is stepped across the whole image resulting in a 2-D cross-correlation map having values on the range of 1 to -1, representing correlated to anti-correlated. This process is shown diagrammatically in Fig. 2.

2.2 *Sample Preparation*

A *Xenopus laevis* (African frog) tadpole of development-stage 41, 6 days postfertilization was imaged. The *Xenopus laevis* tadpole is commonly used in developmental biology studies and recent examples of OCT imaging of the tadpole include demonstration of retinal degradation, cellular level imaging, vascular morphology and video-rate blood flow imaging. A healthy *Xenopus laevis* was primed with 50 μl of human chorionic gonadotropin (HCG) a week before the *in vitro* fertilization (IVF). A day before the IVF, the *Xenopus* was injected with 800 μl of HCG. *Xenopus laevis* IVF was done using standard lab protocol. The IVF *Xenopus* embryo was initially grown at 17°C inside an incubator with 0.1M modified Barth's saline buffer until stage 13, and then the temperature was increased to 25°C from stage 13 onward. The tadpole was anesthetized with tricaine mesylate (0.01% of MSS-222, pH 7.4) in order that it remained still during imaging. At stage 42 and 6 days postfertilization of the tadpole's development, the blood vessels can clearly be seen even with conventional microscopy due to the high transparency of the surrounding tissue.

3 Results and Discussions

A glass capillary with an internal diameter of 300 μm (outer diameter = 400 μm) was filled with 5% intralipid solution and embedded into a synthetic clay [Blu-Tac (R), Bostic Wauwatosa, Wisconsin] in order to simulate the background heterogeneity of tissue. The solution was allowed to move under Brownian motion and the beam was focused to an approximate depth of 80 μm into the capillary. A total of 100 images were acquired at a frame rate of 10 Hz over a time period of 10 s with an exposure time of 10 ms. The exposure time was maximized for each scan so that the maximum intensity was just below the saturation point of the camera-sensor. Figure 3(a) shows the microscope image (taken with the reference arm closed) of the glass capillary. The saturated region in the center is caused by the Fresnel reflection from the top surface of the capillary. Figure 3(b) shows a demodulated *en face* image of the phantom. The reflected intensity from the clay is approximately equal to that of the solution; however, over time, the time-varying speckle is clearly visible. The correlation mapping algorithm is applied to the *en face* images and the corresponding cmOCT image is shown in Fig. 3(c). In this image, it can clearly be seen that the light reflections from the static region [marked as "S" in Fig. 3(b)] remains correlated. The dynamic scatterers [region marked as "D" in Fig. 3(b)] cause a reduction in the correlation between consecutive frames and hence a significant contrast between the two regions is observed. Movie clips are provided for Figs. 3(a)–3(c).

In vivo imaging of a *Xenopus laevis* tadpole was also performed with the tail region placed on a glass slide while the head of the tadpole was kept in water (water anaesthetic solution). The sample beam was focussed on the tail region to a depth of ~100 μm. A series of images were acquired at a rate of 10 Hz over a period of ten seconds giving a total of 100 frames with an exposure time of 15 ms. A microscope image (image taken with the reference arm closed) is shown in Fig. 4(a).

The mean *en face* image is shown in Fig. 4(b) clearly showing the dorsal longitudinal anastomosing vessel (DLAV), the dorsal aorta (DA), and the posterior cardinal vein (PCV).[13] Again, over time, the time-varying speckle caused by the blood moving through the blood vessels is clearly observable. An example of a single cmOCT image is shown in Fig. 4(c). The PCV and the DA are clearly distinguished. Movie clips are provided for Figs. 4(a)–4(c). Figure 4(d) shows a 3-D rendering at a similar location of the tail region. The volume is reconstructed from of a series of *en face* images taken at 2-μm intervals over a depth of 100 μm. Figure 4(e) shows the corresponding volume reconstructed from the cmOCT images. Figure 4(f) shows a Y–Z slice of the *en face* volume taken at the position marked by the red plane. Similarly, Fig. 4(g) shows a Y–Z slice of the cmOCT volume taken at the position marked by the red plane.

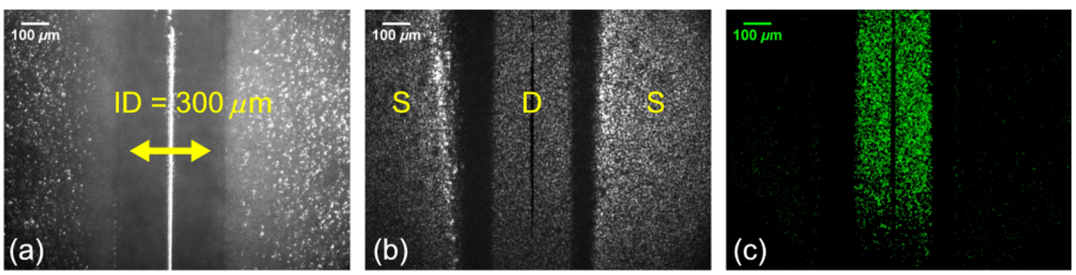

Fig. 3 (a) Microscope image of a phantom consisting of a glass capillary containing 5% intralipid solution. The internal diameter (marked "ID") of the capillary is 300 μm. (b) An *en face* image of the capillary. The intralipid solution moves under Brownian motion (region marked "D") and the static regions are marked "S." (c) The corresponding cmOCT image of the phantom. Videos 1 (MOV, 10.0 MB) [URL: http://dx.doi.org/10.1117/1.JBO.18.12.126008.1], 2 (MOV, 10.1 MB) [URL: http://dx.doi.org/10.1117/1.JBO.18.12.126008.2], and 3 (MOV, 9.99 MB) [URL: http://dx.doi.org/10.1117/1.JBO.18.12.126008.3] corresponding to (a), (b), and (c) are also provided.

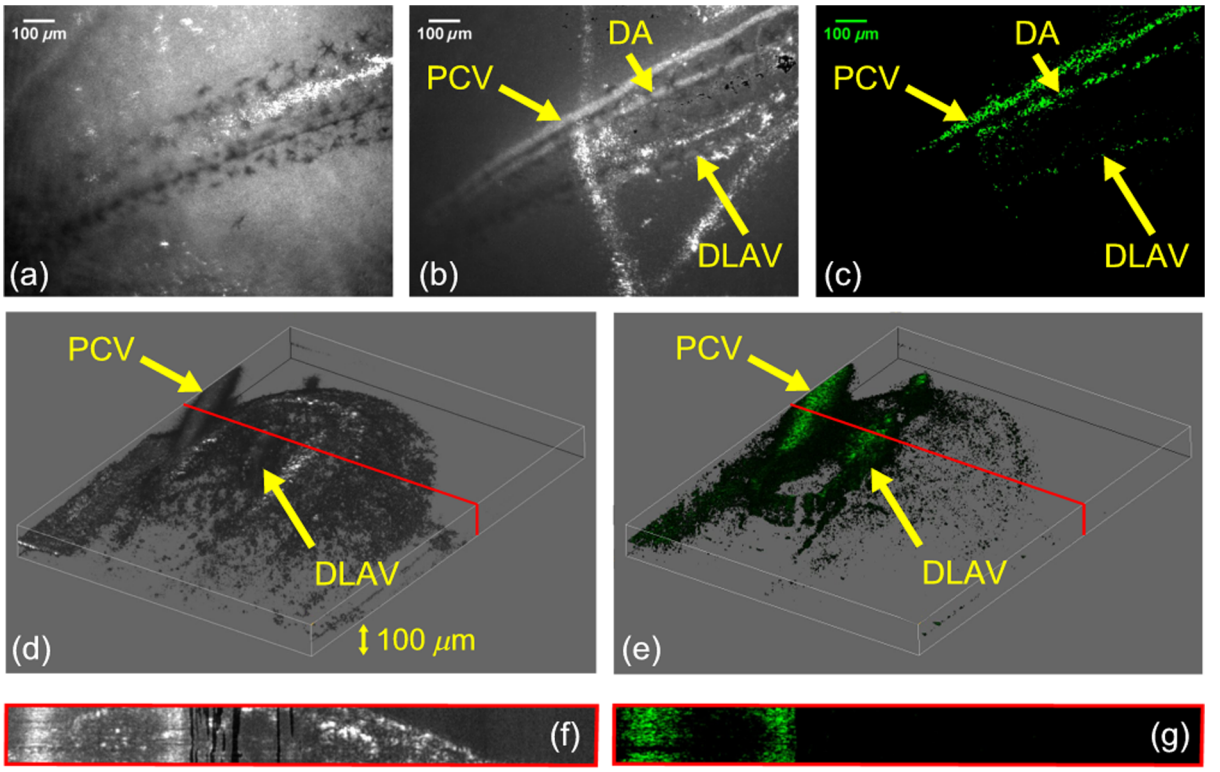

Fig. 4 (a) Microscope image of the tail region of a stage 42 (6 days postfertilization) *Xenopus* tadpole. (b) The mean *en face* image showing the dorsal longitudinal anastomosing vessel (DLAV), the dorsal aorta (DA) and the posterior cardinal vein (PCV). (c) The corresponding cmOCT image. Videos 4 (MOV, 10.0 MB) [URL: http://dx.doi.org/10.1117/1.JBO.18.12.126008.4], 5 (MOV, 10.0 MB) [URL: http://dx.doi.org/10.1117/1.JBO.18.12.126008.5], and 6 (MOV, 9.88 MB) [URL: http://dx.doi.org/10.1117/1.JBO.18.12.126008.6] corresponding to (a), (b), and (c) are also provided. (d) Three-dimensional (3-D) scan of the tail region reconstructed from *en face* images. (e) The corresponding 3-D scan reconstructed from cmOCT images. (f) Y–Z slice of the *en face* volume taken at the position of the red plane. (g) Y–Z slice of the cmOCT volume taken at the position of the red plane.

4 Summary

This work has illustrated the feasibility of applying the cmOCT algorithm to the full-field modality of OCT for the purpose of utilizing the time-varying speckle effect as a contrast mechanism between static and dynamic scatterers. A tissue-mimicking phantom was created and it was shown that Brownian motion in intralipid solution caused a reduction in correlation of the signal-intensity in successive frames at 10 Hz. Hence, a significant contrast between dynamic and static regions was provided, highlighting the system's sensitivity to flow. *In vivo* imaging of the microvasculature of a tadpole at development-stage 46 was performed showing good contrast between regions of blood flow and static tissue.

Acknowledgments

The authors wish to acknowledge the generous help from Santosh Kumar Maharana and Dr. Gerhard Schlosser of the School of Natural Science, National University of Ireland, Galway.

References

1. D. Huang et al., "Optical coherence tomography," *Science* **254**(5035), 1178–1181 (1991).
2. E. Beaurepaire et al., "Full-field optical coherence microscopy," *Opt. Lett.* **23**(4), 244–246 (1998).
3. S. Chang et al., "Full-field optical coherence tomography and its application to multiple-layer 2D information retrieving," *Opt. Commun.* **246**(4–6), 579–585 (2005).
4. A. Dubois et al., "Three-dimensional cellular-level imaging using full-field optical coherence tomography," *Phys. Med. Biol.* **49**(7), 1227–1234 (2004).
5. H. M. Subhash, "Full-field and single-shot full-field optical coherence tomography: a novel technique for biomedical imaging applications," *Adv. Opt. Technol.* **2012**(2012), 26 (2012).
6. M. Akiba and K. Pui Chan, "*In vivo* video-rate cellular-level full-field optical coherence tomography," *J. Biomed. Opt.* **12**(6), 064024 (2007).
7. M. S. Hrebesh, R. Dabu, and M. Sato, "*In vivo* imaging of dynamic biological specimen by real-time single-shot full-field optical coherence tomography," *Opt. Commun.* **282**(4), 674–683 (2009).
8. J. Qu and H. Niu, "Study of reconstruction algorithms for phase-stepped full-field optical coherence tomography," *Jpn. J. Appl. Phys.* **45**(5A), 4256–4258 (2006).
9. J. Na et al., "Image restoration method based on Hilbert transform for full-field optical coherence tomography," *Appl. Opt.* **47**(3), 459–466 (2008).
10. E. Jonathan, J. Enfield, and M. J. Leahy, "Correlation mapping method for generating microcirculation morphology from optical coherence tomography (OCT) intensity images," *J. Biophotonics* **4**(9), 583–587 (2011).
11. J. Enfield, E. Jonathan, and M. Leahy, "*In vivo* imaging of the microcirculation of the volar forearm using correlation mapping optical coherence tomography (cmOCT)," *Biomed. Opt. Express* **2**(5), 1184–1193 (2011).
12. A. Zam et al., "Feasibility of correlation mapping optical coherence tomography (cmOCT) for anti-spoof sub-surface fingerprinting," *J. Biophotonics* **6**(9), 663–667 (2013).
13. A. J. Levine et al., "Fluorescent labeling of endothelial cells allows in vivo, continuous characterization of the vascular development of Xenopus laevis," *Dev. Biol.* **254**(1), 50–67 (2003).